Impact on floating membranes

Nicolas Vandenberghe[*] and Laurent Duchemin[†]

Aix Marseille Université, CNRS, Centrale Marseille, IRPHE UMR 7342, F-13384 Marseille, France

When impacted by a rigid body, a thin elastic membrane with negligible bending rigidity floating on a liquid pool deforms. Two axisymmetric waves radiating from the impact point propagate. First, a longitudinal wave front, associated with in-plane deformation of the membrane and traveling at constant speed, separates an outward stress-free domain from a stretched domain. Then, in the stretched domain a dispersive transverse wave travels at a speed that depends on the local stretching rate. The dynamics is found to be self-similar in time. Using this property, we show that the wave dynamics is similar to the capillary waves that propagate at a liquid-gas interface but with a surface tension coefficient that depends on impact speed. During wave propagation, we observe the development of a buckling instability that gives rise to radial wrinkles. We address the dynamics of this fluid-body system, including the rapid deceleration of an impactor of finite mass, an issue that may have applications in the domain of absorption of impact energy.

I. INTRODUCTION

The impact of a solid sphere on a liquid surface is a scientific problem that has attracted considerable interest since the early observations of Worthington [1] of the dynamics of the cavity formed in the wake of the sphere. This problem has recently attracted a renewed interest, and the cavity dynamics has been studied in detail by various authors [2,3]. Water entry is indeed an important problem for various applications, including aerospace science [4], where plane impacts have served as an early motivation [5,6], naval engineering [7], and, more recently, animal locomotion [8].

In most of the applications cited above, the force exerted on the impacting body by the fluid results mainly from an inertial response. This means that other types of effects such as surface tension, gravity, or viscosity are negligible. For an object of characteristic size r_i impacting on a liquid surface (density ρ, kinematic viscosity ν, surface tension σ) with a velocity V, the Weber number that measures the ratio between inertia and surface tension $\mathrm{We} = \rho r_i V^2 / \sigma$ and the Reynolds number $\mathrm{Re} = V r_i / \nu$ are very large in the context of these applications.

The case of small Weber numbers, i.e., surface-tension-dominated impacts, has also been studied in the context of the locomotion of small organisms [8,9]. Small Weber numbers are obtained for small objects or when the surface tension is large. The latter situation is encountered in particular when an elastic membrane is at the interface between the liquid and the gas like for a liquid-filled rubber balloon [10]. In this case, the tension in the thin rubber membrane results from the internal pressure in the balloon, and it can be several orders of magnitude larger than the typical value for the water-air interface. Provided that the initial tension is large and the amplitude of the motion of the surface of the balloon is small, the analogy with a liquid-gas interface is straightforward. However, in the general case, the tension in the membrane varies with its local strain typically through Hooke's law. Therefore the surface tension coefficient is, in general, not constant and not uniform: it is a dynamical variable that changes with the longitudinal (tangential) motion of the membrane. Similar situations are encountered in the case of liquid-gas interfaces in the presence of surfactants, where longitudinal motion at the interface may change the local concentration of surfactants and thus the surface tension [11–14].

In the present paper, we investigate a situation in which a floating membrane acts locally like an interface with a very large surface tension coefficient compared to a liquid-gas interface, such that, for our experiments, the Weber number is smaller than 1. The Reynolds number is still very large, which allows us to neglect viscous effects. Gravity can also be neglected. The membrane is initially flat and tension free (the small background stress imposed by the liquid-air surface tension at the side of the membrane can be neglected). In this case the surface tension coefficient is not known *a priori*. It results from a coupling between the transverse motion (throughout the text, transverse refers to the direction normal to the interface) resulting from the impact and the stretching of the membrane that builds up following the impact. Because of this coupling and because the background stress is negligible, the problem is considerably more difficult than the classical problem of wave propagation on stretched membranes [15]. In the absence of a liquid substrate, the dynamics has been investigated by various authors in the context of ballistic impacts [16–18]. These studies have shown that the displacement in the plane of the membrane and the transverse displacement are strongly coupled and need to be considered concomitantly. Furthermore the analysis has shown that the axisymmetric wave propagation can be unstable and that wrinkles resulting from a buckling instability appear.

In a recent paper [19], we investigated the two-dimensional problem of a thin floating membrane, made of natural rubber, being impacted by a horizontal metal rod. In this context, the stretching response of the membrane is of the same nature as liquid-gas surface tension but shows a surface tension coefficient increasing linearly with the impact velocity. This two-dimensional coupled dynamics between the membrane and the liquid (water) on which it floats exhibits self-similar solutions like the ones observed for a liquid-gas interface [20]. This

---

[*]vandenberghe@irphe.univ-mrs.fr
[†]duchemin@irphe.univ-mrs.fr

surprising fact results from the uniform state of strain in the membrane, allowing for a straightforward analogy between an impacted membrane and a liquid-gas interface. In the present paper, we investigate axisymmetric situations, for which the simplification of a uniform membrane stretching does not hold. Indeed, when a metal ball or a vertical cylinder impacts the membrane, the resulting strain in the membrane, and therefore the related stresses, is highly nonuniform, as we shall see.

This paper is organized as follows: in Sec. II we describe the experiments and the phenomenology of the impacted membrane. In particular we emphasize the propagation of two distinct waves, a wave associated with the in-plane motion of material points of the membrane that is decoupled from the hydrodynamics and a transverse wave that is accompanied by fluid motion. The wave dynamics is addressed in details in Sec. III; then the static membrane equations are solved numerically in Sec. IV in order to analyze the scaling for the strain observed in the experiments. Section V discusses the wrinkling instability of the membrane that develops as the waves propagate, and Sec. VI discusses the deceleration of the impactor.

II. EXPERIMENTS

A. Setup

A steel impactor with a hemispherical head of radius $r_i = 0.75$ or 1.5 or 2.5 mm impacts transversally a thin rubber membrane (thickness H in the range 0.15 to 0.30 mm) floating at the surface of a water tank of dimensions $40 \times 40 \times 40$ cm. Impactors are accelerated by gravity or by a gas gun, and they impact the membrane at speeds in the range 0.3 to 30 m/s. Experiments addressing the wave dynamics (in particular at low impact speeds) are conducted with impacting cylinders

that are sufficiently heavy to ensure that the impactor does not decelerate during the experiment. The membrane is a circular or square sheet with a typical dimension (diameter or side length) of 15 cm. The shape of the membrane is not relevant since we focus on short-time dynamics before waves have had time to interact with the boundary. The typical duration of an experiment is less than 10 ms, and the dynamics is recorded with a high-speed camera at typical frame rates of 10 000 frames per second.

The membrane is characterized by a stretching modulus $Y = E'H$, with $E' = E/(1 - \nu^2)$, where E is Young's modulus, $\nu = 1/2$ is the Poisson ratio, and H is the thickness of the membrane in the reference state. The natural rubber used in the experiments has a Young modulus $E = 2.6$ MPa, and a stretching rate of 500% or more can be reached. For simplicity and since most of the dynamics occurs at low stretching (below 10% except in a small area near the impactor), we will assume that the material response can be accurately described by Hooke's law (see [21] for references to more complex models in the context of impacts). A typical value of the stretching modulus is 720 N/m. Thus, even for low strains ϵ of the order of 10^{-3}, the stresses induced by strains $Y\epsilon$ are orders of magnitude larger than the stress resulting from surface tension at the liquid-air interface, and the latter will be neglected throughout this work.

B. Phenomenology

After impact, two waves propagate on the membrane (Fig. 1). They are clearly seen on a spatiotemporal diagram showing the position of material points as a function of time. A material point located at a distance R from the impact point is first reached by a longitudinal wave front. Behind this wave front, the material points move in the plane of
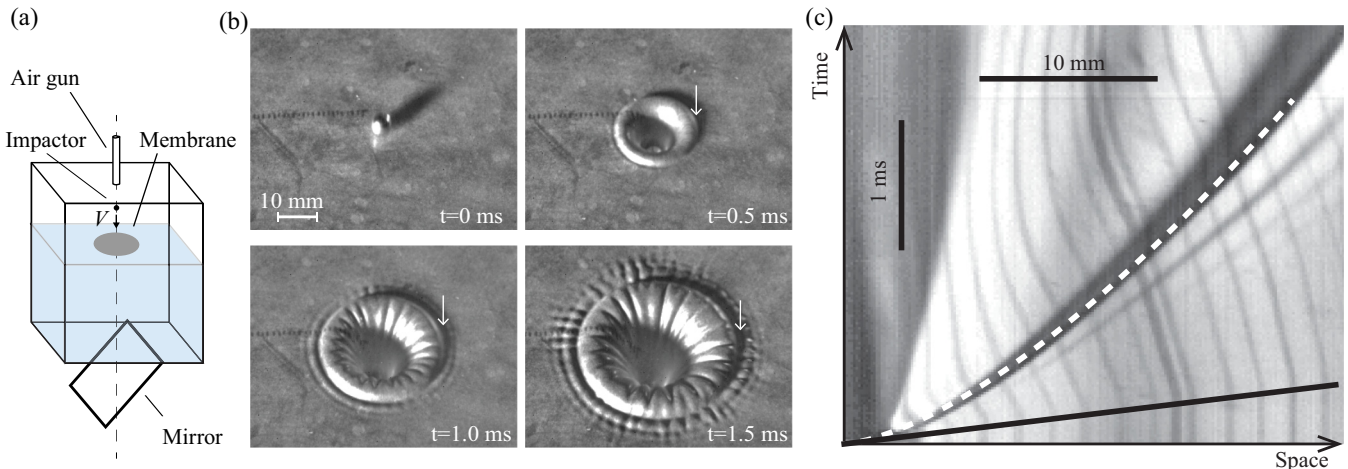

FIG. 1. (a) Sketch of the experiment. (b) Successive snapshots of a floating membrane (thickness $h = 0.2$ mm) made of natural rubber impacted by a solid sphere. The extension of a cavity delimited by a transverse wave front is accompanied by the development of a wrinkling instability both inside and outside the cavity. (c) A spatiotemporal diagram of the motion of the material points along a radius of a membrane impacted at $V = 31.2$ m/s obtained by recording the movie from below the surface. Marks drawn on the membrane reveal the motion of the material points. Two waves can be seen: a longitudinal wave separates a domain where material points are at rest from a domain where they move towards the impact point. The longitudinal wave front travels at the speed $c = 60$ m/s (solid line). The dark shadow highlighted by the dashed white line corresponds to the positions marked by the arrow in (b). This transverse wave front travels at nonconstant speed. The dashed line is the line $a't^{2/3}$, with $a' = 13.2$ mm ms$^{-2/3}$.
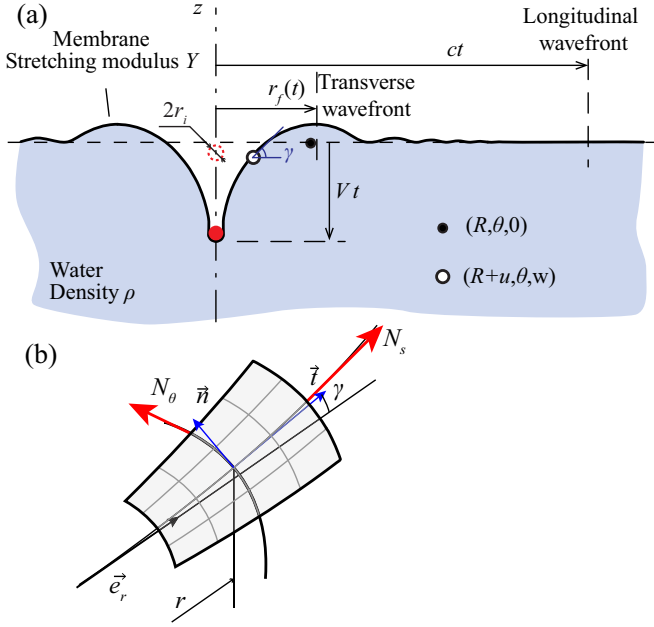
FIG. 2. (a) Sketch of the impacted membrane and definition of the length r_f. (b) Notations for the model.

the membrane towards the impact point. The displacement is radial and is denoted $u(R,t)$. At later times, the material points move in the transverse direction, with the transverse displacement being denoted $w(R,t)$, experiencing first an oscillation of growing amplitude and later a strong transverse motion first upward and then downward towards the liquid. The wave front associated with the longitudinal motion travels at constant speed [Fig. 1(b)]. Behind this longitudinal wave front, the membrane is stretched in a nonuniform manner: the stretching increases towards the impact point. The transverse wave front travels in the stretched domain. The out-of-plane displacement occurs in an area well delimited by a hump, which we use to define $r_f(t)$ [see Fig. 2(a)]. The transverse wave front travels at a speed that decreases with time, and its position is well approximated by the law $r_f(t) \sim at^{2/3}$ [Fig. 1(b)]. This scaling is typical of surface-tension-driven flows, and it has been observed for two-dimensional impacts on membranes [9,19,20]. The coefficient a changes with the impact speed. This wave dynamics will be discussed in the next section.

During its extension, the axisymmetric wave pattern presents an instability, and radial wrinkles appear, as seen in Fig. 1(b). Such patterns appear frequently on elastic membranes which are not able to withstand compressive in-plane stresses [22,23]. Inside the cavity, wrinkles develop on the curved membrane. The number of wrinkles does not change as the cavity extends, and the wrinkles extend from the vicinity of the contact with the impactor to the ridge of the cavity. Outside of the cavity, radial wrinkles are also present but their number is different from the number of wrinkles inside the cavity. We note that there is a transition area between the cavity and the outer domain on which wrinkles are not observed.

III. WAVE DYNAMICS

The longitudinal wave front that travels first in the membrane does so at a constant speed $c = 60$ m s^{-1}, independent of the impact speed. The transverse wave front travels with a well-defined law $r_f(t) = at^{2/3}$, where the constant a increases with the impact velocity (Fig. 3). Here the membrane plays the role of an interface with a surface tension coefficient σ given by the local tension resulting from stretching. Therefore, in analogy with surface-tension-driven flows, we write for r_f

$$r_f(t) = at^{2/3} = \left(\alpha \frac{Y\epsilon_f}{\rho}\right)^{1/3} t^{2/3}, \qquad (1)$$

where $\epsilon_f = \epsilon_s|_{r_f}$ is the radial strain in $r = r_f(t)$ and α is an order 1 number. $\sigma = Y\epsilon_f$ is the local tension (with the dimension of a force per unit length) in the membrane: it plays the role of surface tension. Measurements of the position of the transverse wave front (Fig. 3) suggest that the prefactor a is, to a good approximation, constant in time or at least exhibits a very slow variation compared to $t^{2/3}$. Therefore ϵ_f should be constant in time. Direct measurement of the strain $\epsilon_s = (\ell - \ell_0)/\ell_0$ was performed by tracking two neighboring material points drawn on the membrane and measuring the current distance ℓ (ℓ_0 is the distance in the undeformed state). The strain ϵ_s measured in r_f is roughly constant (inset of Fig. 4). From these observations, we conclude that the membrane behaves locally, i.e., in $r = r_f(t)$, as a liquid-gas interface, with a surface tension coefficient $Y\epsilon_f$.

We observe in the experiments that both the coefficient a^3 obtained by measuring the position of the wave front and the strain in $r = r_f$ measured by tracking material points ϵ_f scale like We$^{1/3}$ (Fig. 4), where

$$\text{We} = \frac{\rho r_i V^2}{Y} \qquad (2)$$

is the Weber number. As in the two-dimensional case [19], the local strain ϵ_f depends on the impact velocity, and we shall study this dependence in Sec. IV.
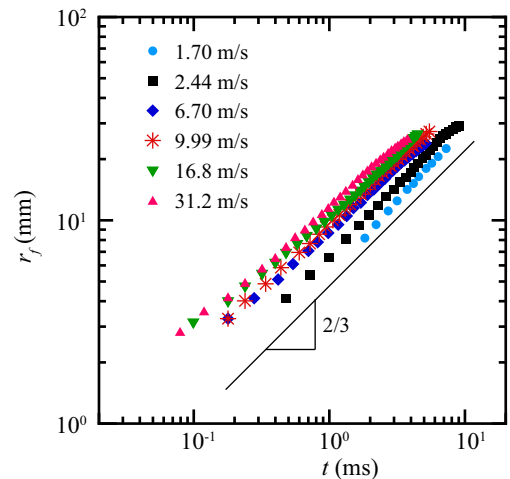

FIG. 3. Positions of the transverse front for different impact speeds for a membrane of thickness $h = 0.21$ mm struck by an impactor of radius $r_i = 2.5$ mm. The scaling law $r_f = at^{2/3}$ is robust with a coefficient a increasing with the impact speed.
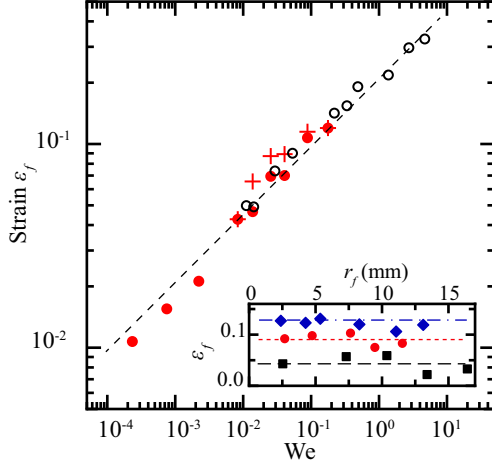
FIG. 4. The strain $\epsilon_f \equiv \epsilon_s(r_f)$ as a function of Weber number We $= \rho r_i V^2/Y$. The red crosses correspond to direct measurements of the strain at r_f obtained by tracking the position of material points. The circles and disks correspond to the strain inferred from the prefactor a obtained from the fit $r_f = at^{2/3}$. The strain is $\epsilon_f = (1/\alpha)\rho a^3/Y$, where the coefficient $\alpha = 6.1$ is chosen to match the direct measurements of ϵ_f. Red disks correspond to impacts on a membrane of thickness $h = 0.14$ mm with an impactor of radius $r_i = 0.75$ mm (the same conditions as the red crosses). The black circles correspond to impacts on a membrane of thickness $h = 0.21$ mm struck by an impactor of radius $r_i = 2.5$ mm (the data of Fig. 3). The dashed line is a fit of the experimental data $\epsilon_f = \delta \, \text{We}^{1/3}$, with $\delta = 0.22$. The inset shows the direct measurements of the strain in r_f for different times (and thus different r_f) at different impact speeds (black squares, $V = 1.9$ m/s; red disks, $V = 4.3$ m/s; blue diamonds, $V = 9.0$ m/s). The strain ϵ_f is constant.

The experiments also show that, for sufficient impact speeds or for long times, the transverse displacement $w(r,t)$ is a self-similar profile of the form

$$w(r,t) = \eta r_f(t) W\left(\frac{r}{r_f(t)}\right), \qquad (3)$$

where η depends on impact speed V. This scaling is also characteristic of surface-tension-driven flows [20].

Figure 5 shows experimental profiles of one experiment, rescaled according to $at^{2/3}$ (with a determined in the experiment) in both directions r and z. A unique curve is obtained away from the impactor. In the impactor region, the scaling of Eq. (3) does not hold since the vertical displacement is Vt, neglecting the deceleration of the impactor. The matching condition at the impactor $-Vt = w(r_i,t)$ imposes the behavior of the function W for small r. To obtain linearity with time, it follows that $W(x) \sim -x^{-1/2}$, and choosing $\eta = V r_i^{1/2}/a^{3/2}$, we find for $r_i/r_f \to 0$

$$w(r_i,t) \simeq -\frac{V r_i^{1/2}}{a^{3/2}} \frac{r_f}{(r_i/r_f)^{1/2}} = -Vt. \qquad (4)$$

Despite these observations, the complete analogy with surface-tension-driven flows is not straightforward because the strain ϵ_s in the membrane is not uniform, as seen in Fig. 6. Indeed, the stretching ϵ_s is large near the impactor and decreases rapidly as r increases. Thus a detailed description of
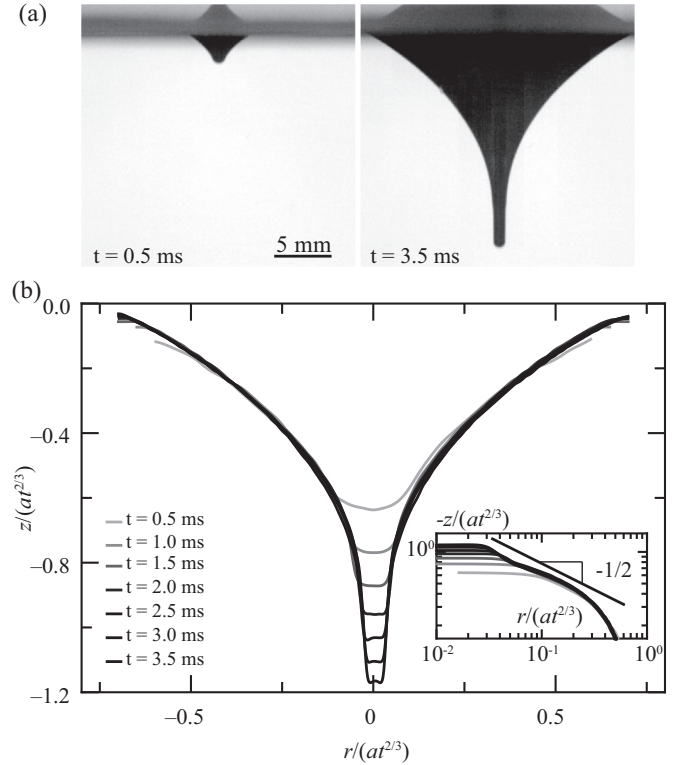

FIG. 5. (a) Shape (profile) of the membrane for an impactor of radius $r_i = 0.5$ mm impacting at $V = 5.6$ m/s a membrane of thickness $h = 0.2$ mm. (b) Experimental profiles for which r and z coordinates have been rescaled by $at^{2/3}$, with $a = 7.3$mm/ms$^{2/3}$, show a self-similar behavior. Inset: The self-similar profiles shown in log-log scales. The matching of the self-similar profile with the boundary condition in $r = r_i$ imposes the shape of the profile $w \sim r^{-1/2}$ for $r \ll 1$.

the full dynamics, including the fluid and the membrane, must be sought to obtain a description of the wave dynamics and, in particular, to address the variation of the coefficient a with impact speed.

IV. SCALING FOR THE STRAIN

A. The response of a membrane to transverse impact

To gain better insight into the dynamics of the fluid-body coupled system and, in particular, to address the relation between the coefficient a and the Weber number We, we propose a model that couples the motion of the deformable membrane with the motion of the underlying fluid. We make the usual assumptions of wave theory (inviscid and irrotational flow of an incompressible fluid) for which we can use the velocity potential $\phi(r,z,t)$. We assume that the membrane plays the role of an interface and that it can be described as an infinitely thin sheet whose position is denoted $w(r,t)$ (Fig. 2). At this stage we assume that the problem is axisymmetric. The velocity potential verifies the continuity equation $\Delta\phi = 0$ in the fluid domain. At the interface, $z = w(r,t)$, the kinematic boundary condition reads

$$\partial_t w + \partial_r w \, \partial_r \phi = \partial_z \phi. \qquad (5)$$

(a)

$t=0$ $t=0.5$ ms $t=1$ ms
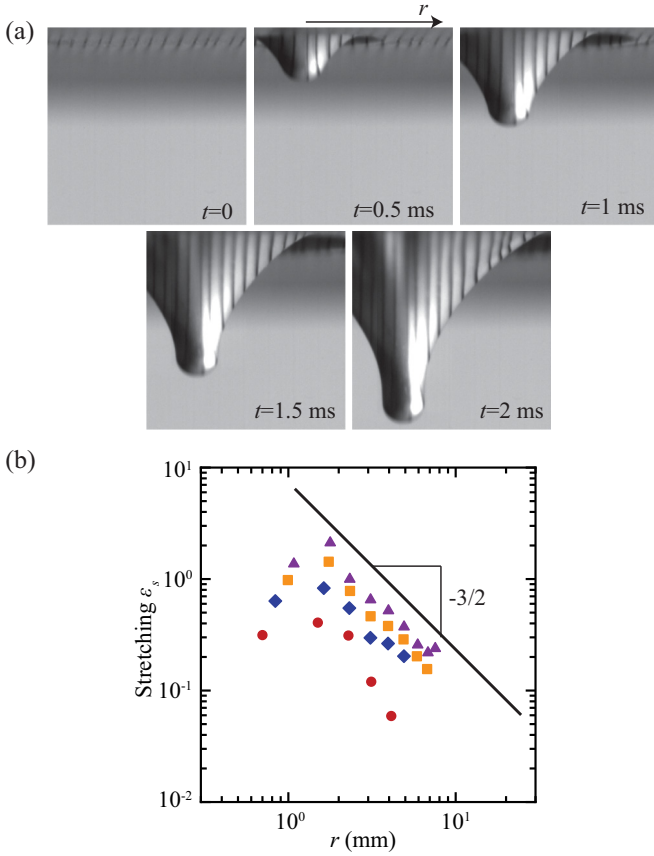
$t=1.5$ ms $t=2$ ms

(b)

FIG. 6. (a) Successive profiles showing the motion of material points. The stretching is higher near the impactor. In this experiment, the radius of the impactor is $r_i = 1.5$ mm, the thickness of the elastic sheet is $h = 0.2$ mm, and the impact velocity is $V = 6.6$ m/s, corresponding to We $= 9.1 \times 10^{-2}$. (b) Variations of the stretching ϵ_s with r for the pictures in (a). Time increases from bottom to top.

The dynamic boundary condition (gravity is neglected) reads

$$\partial_t \phi + \frac{1}{2}|\boldsymbol{\nabla}\phi|^2 + \frac{p}{\rho} = 0, \qquad (6)$$

where p is the pressure difference across the membrane.

In the reference (undeformed) configuration, the membrane is flat, and a material point has coordinates $(R,\theta,0)$ in cylindrical coordinates [black dot in Fig. 2(a)]. After deformation, the position is denoted by (r,θ,z) [white dot in Fig. 2(a)]. The displacements are $u = r - R$ in the radial direction and $w = z$ in the vertical direction. The equations of motion for an element $hr\,ds\,d\theta$ of a membrane of mass $\rho_s h r\,ds\,d\theta$ experiencing a pressure difference p across its normal and forces per unit length N_s and N_θ in the radial and orthoradial directions along the radial and vertical directions read

$$\rho_s h r \frac{\partial^2 u}{\partial t^2} = -pr\sin\gamma + \frac{\partial}{\partial s}(N_s r \cos\gamma) - N_\theta, \qquad (7)$$

$$\rho_s h r \frac{\partial^2 w}{\partial t^2} = pr\cos\gamma + \frac{\partial}{\partial s}(N_s r \sin\gamma), \qquad (8)$$

where s is the curvilinear coordinate along a meridian line and the angle γ is given by

$$\cos\gamma = \frac{\partial r}{\partial s}, \quad \sin\gamma = \frac{\partial w}{\partial s}. \qquad (9)$$

The strains in the radial and orthoradial directions are

$$\epsilon_s = \frac{\partial s}{\partial R} - 1, \quad \epsilon_\theta = \frac{r}{R} - 1. \qquad (10)$$

From the relation $r = R(1 + \epsilon_\theta)$, one obtains after some algebra a compatibility equation

$$\frac{r}{1+\epsilon_\theta}\frac{d\epsilon_\theta}{dr} + \frac{1+\epsilon_\theta}{1+\epsilon_s}\frac{1}{\cos\gamma} = 1. \qquad (11)$$

To describe the longitudinal wave that propagates ahead of the transverse perturbation, we first consider the case of in-plane displacement, with $w = 0$, for which the motion of the membrane is not coupled to the fluid (because viscous effects are neglected). Then $\gamma = 0$ and assuming Hookean behavior of the membrane,

$$N_s = Y(\epsilon_s + \nu\epsilon_\theta), \quad N_\theta = Y(\epsilon_\theta + \nu\epsilon_s), \qquad (12)$$

Eq. (7) reads, in the limit of small strains, i.e., for $|\epsilon_\theta| = |u/R| \ll 1$,

$$\frac{1}{c^2}\frac{\partial^2 u}{\partial t^2} = \frac{1}{R}\frac{\partial}{\partial R}\left(R\frac{\partial u}{\partial R}\right) - \frac{u}{R^2}, \qquad (13)$$

with $c^2 = (E'/\rho_s)$. This equation describes the propagation of a longitudinal (i.e., in-plane) perturbation at speed c, which is a material constant, in quantitative agreement with the experiment [Fig. 1(b)].

The full set of equations coupling the membrane and fluid equations cannot be solved analytically. To gain insight into the physics of the waves we make the following simplifications: (i) we neglect the left-hand side in Eq. (7); that is, we consider that the in-plane stresses are at equilibrium up to $r = ct$. (ii) We also neglect the left-hand side in Eq. (8) in comparison with the fluid inertia (a hypothesis that is valid for waves with a wavelength larger than the thickness of the membrane). We obtain the following set of equations for the membrane:

$$p + \frac{1}{r}\frac{\partial}{\partial r}(N_s r \sin\gamma) = 0, \qquad (14)$$

$$\frac{d}{dr}[rN_s] - N_\theta = 0. \qquad (15)$$

Equations (14) and (15) are the normal and tangential equilibrium equations for the membrane element, respectively. Equation (14) is also a dynamic boundary condition for the fluid motion, coupled with Bernoulli equation (6) through the pressure p. We note that assumption (ii) cannot be made in the absence of fluid. The case of the impact on a free membrane has been addressed before [16–18].

It is instructive to consider the case of a constant and uniform tension N_s. The fluid pressure is related to the shape of the membrane through

$$p + N_s\left(\frac{d\gamma}{ds} + \frac{\sin\gamma}{r}\right) = 0, \qquad (16)$$

which is precisely Laplace's law. Therefore the analogy with surface-tension-driven flows [20] is straightforward. In

particular, dimensional analysis reveals that at time t after impact the characteristic length scale associated with the propagation of the transverse wave reads $at^{2/3} \sim (N_s t^2/\rho)^{1/3}$. Such analogy cannot be used in the general case of a nonuniform membrane stress.

B. Approximate solution

We first remark that the full system of equations (5), (6), and (11)–(14), together with mass conservation in the fluid bulk $\Delta\phi = 0$, can be written using a self-similar ansatz for which all the terms balance in the equations, apart from the boundary condition in $r = r_i$. The ansatz for the transverse displacement and the two strains are

$$w(r,t) = \eta r_f W(\xi), \quad \epsilon_s = E_s(\xi), \quad \epsilon_\theta = E_\theta(\xi), \quad (17)$$

where $\xi = r/r_f$ and $r_f = at^{2/3}$. The use of the same self-similar ansatz for all the fields is dictated by the fact that the strain ϵ_s has to be a constant in the region of r_f in order for a to be a constant. Using the fact that $\tan\gamma = \partial w/\partial r = \eta W'(\xi)$, the full system of self-similar equations is given in the Appendix.

This reduction to a self-similar system provides a clue as to why a scaling $r_f = at^{2/3}$ is observed. However, there are a few difficulties associated with this approach. First, the boundary conditions at $r = r_i$ and $r = ct$ are not self-similar. This means that a self-similar solution with the scalings (17) will not verify the boundary conditions, particularly the boundary condition $w(r_i,t) = -Vt$, which is fundamental in the present problem. Another difficulty associated with the self-similar approach is that it does not provide a scaling for the strain. In particular, the dependence of the strain in $r = r_f$ on the impact speed cannot be determined without computing the full solution of the problem, which remains a formidable task. We propose in this section a simplified analysis.

In order to explore the main features of the wave dynamics, the constant character of the strain in r_f and its scaling with the impact speed, we have solved the quasistatic membrane equations (11) and (15), using a profile w compatible with the observed self-similar shape (3). Therefore a solution to the equation for the transverse position (14) was not sought. We choose the form

$$w(r,t) = -\eta r_f \frac{\sin(Ar/r_f)}{A(r/r_f)^{3/2}}, \quad (18)$$

where $A = 4.38$, such that the first maximum is located at $r = r_f$. Apart from the self-similarity, this shape, especially the behavior $w(r,t) \sim r^{-1/2}$ for small r, was chosen such that the boundary condition in r_i [Eq. (4)] is satisfied. Our simplified approach consists of replacing the highly complex coupling between the membrane and the fluid motion with the feature of the flow, built in Eq. (18), that the transverse wave propagates according to $r_f(t) = at^{2/3}$.

Equations (11) and (15) were solved with a shooting technique, imposing the boundary conditions $\epsilon_s(r_i) = \epsilon_\theta(r_i)$ and $\epsilon_\theta(ct) = 0$. The solution is shown in Fig. 7. The same physical parameters as in the experiment presented in Fig. 5 have been used, and the equations were solved for the same seven times. Figure 7(a) shows the values of ϵ_s in r_i, r_f, and ct as a function of the rescaled time Vt/r_i. To a good
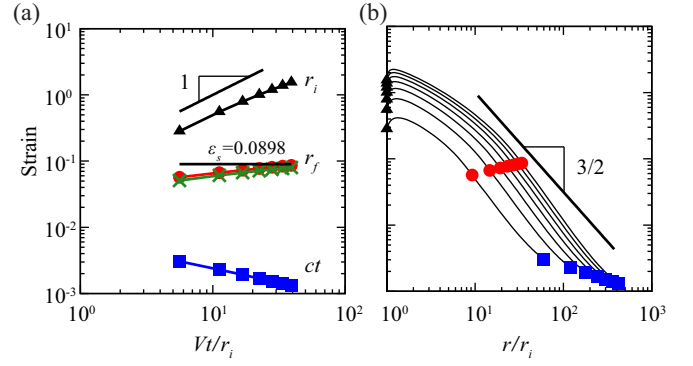

FIG. 7. (a) Longitudinal strains ϵ_s (triangles, disks, and squares) measured in $r = r_i$, r_f, and ct, when solving equations (15) and (11), as a function of the dimensionless time Vt/r_i. The crosses correspond to the hoop strain ϵ_θ in r_f. The parameters used in the simulation are similar to those of Fig. 5. Note that the strain ϵ_s in r_f varies slowly with time and its value shows quantitative agreement with the value 9.0×10^{-2} expected from the experiment. (b) Longitudinal strain along the membrane as a function of r/r_i for times corresponding to Fig. 5.

approximation, the strain $\epsilon_s(r_i)$ is linear in time, and $\epsilon_s(r_f)$ is constant. Moreover, rescaling the strain ϵ_s by Vt/r_i leads to the collapse of curves for different times, as seen in Fig. 8. In light of these results and seeking an ansatz with constant ϵ_s in $r = r_f$, compatible with Eq. (17), we choose the following representation for the strain field:

$$\epsilon_s(r,t) = \beta \frac{Vt}{r_i}\left(\frac{r}{r_i}\right)^{-3/2}, \quad (19)$$

where β is a numerical constant, with ϵ_θ admitting a similar form (with a different prefactor). The scaling in $(r/r_i)^{-3/2}$ agrees with the results in Figs. 7(b) and 8 and with the measurements presented in Fig. 6. It is also compatible with the self-similar scaling of Eq. (17): taking $t = (r_f/a)^{3/2}$ in
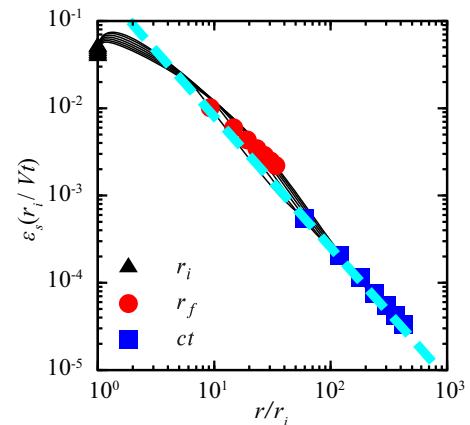

FIG. 8. Longitudinal strain along the membrane, rescaled according to Vt/r_i, as a function of r/r_i, when solving equations (15) and (11). The dashed line corresponds to the function $\beta(r/r_i)^{-3/2}$, where β has been deduced from experimental measurements.

Eq. (19) yields

$$\epsilon_s(r,t) = \beta \frac{V r_i^{1/2}}{a^{3/2}} \left(\frac{r}{r_f} \right)^{-3/2}, \tag{20}$$

which agrees with the form (17).

Moreover, we can use Eq. (20) together with Eq. (1) to obtain

$$\epsilon_f = \left(\frac{\beta^2}{\alpha} \right)^{1/3} \mathrm{We}^{1/3}, \tag{21}$$

which is compatible not only with the experimental fit $\epsilon_f = \delta\, \mathrm{We}^{1/3}$ as a scaling law (as seen in Fig. 4) but also in a quantitative manner through the prefactor. This fact is clearly confirmed in Fig. 8, where the prefactor β has been determined as $\beta = \sqrt{\delta^3 \alpha}$, where $\alpha = 6.1$ and $\delta = 0.22$ are inferred from the experiments (see Fig. 4). Equation (19) with this value for β fits well the numerical values of the strain as a function of r/r_i in a wide region including r_f.

The form (19) is valid in a large domain including r_f but not near the impactor ($r \gtrsim r_i$), as seen in Fig. 8. Looking for a generalization of Eq. (19), we postulate that the strains behave like $\epsilon_s(r,t) = (Vt/r_i)\mathcal{E}_s(r/r_i)$ and $\epsilon_\theta(r,t) = (Vt/r_i)\mathcal{E}_\theta(r/r_i)$. We recall that these time and space dependencies are compatible with the self-similarity observed experimentally, provided the functions $\mathcal{E}_s$ and $\mathcal{E}_\theta$ scale like Eq. (19) in a region enclosing r_f. These observations are consistent with the fact that the strain is constant in time in the vicinity of r_f.

To conclude this section, we recall the main results. The transverse wave front observed in the experiments travels with a well-defined law $r_f(t) = (\alpha Y \epsilon_f t^2/\rho)^{1/3}$, where α is a constant and the strain $\epsilon_f \equiv \epsilon_s(r_f)$ depends on the impact velocity through the scaling law $\epsilon_f = \delta\, \mathrm{We}^{1/3}$. The prefactor δ and the power $1/3$ are experimental observations but are also consistent with a quasistatic membrane solution. This solution of the simplified problem is obtained by imposing a vertical displacement of the impactor $-Vt$ and a self-similar profile (18) compatible with the experiments. Using this analysis of the strain field, we now investigate the wrinkles observed in the experiments.

V. WRINKLING OF THE MEMBRANE

As seen in Fig. 1, as the waves extend, the membrane presents an instability, and wrinkles appear in two distinct domains, for $r < r_f$, where the membrane is out of its plane and is curved, and for $r > r_f$, where the membrane is roughly flat (in its nominal state, i.e., before the instability) but stretched. We treat these domains independently.

A. Wrinkling instability in the flat domain $r > r_f$

The wrinkles that appear outside the cone are also observed in the absence of a liquid substrate [18]. They result from a buckling instability that is caused by the motion of material points towards the impactor in the domain delimited by the longitudinal wave front located in ct and the transverse wave front located in r_f. As a result of the radial motion of the material points, a compressive hoop stress ϵ_θ develops, triggering a buckling instability that gives rise to radial wrinkles. This instability has been described by Vermorel

et al. [18] in the absence of the liquid substrate, and we adapt the analysis to describe the present case. As discussed in Sec. IV, the strain near r_f is roughly constant, with the scaling $\epsilon_\theta \sim \epsilon_s \sim \mathrm{We}^{1/3}$ (Fig. 4). We consider the simple problem of a beam of unit lateral length experiencing a compressive stress $\sigma_\theta = E'\epsilon_\theta < 0$: the beam here represents the unfolded (i.e., uncurved) annulus near the radius $r \gtrsim r_f$. The dispersion relation for a transverse perturbation on the beam [24] (not accounting for added mass) is

$$\rho h \omega^2 = \sigma_\theta h k^2 + \frac{E' h^3}{12} k^4, \tag{22}$$

and the critical wave number is thus given by $hk_c \sim (|\sigma_\theta|/E')^{1/2}$, leading to a wave number of the instability

$$\frac{\lambda}{h} \sim \mathrm{We}^{-1/6}. \tag{23}$$

This result agrees with our observations, as seen in Fig. 9(c). We note also that, as in the absence of substrate, the wrinkling instability selects a wavelength, rather than a number of wrinkles. Thus as the waves propagate, new wrinkles appear (Figs. 1 and 9).

B. Wrinkling instability in the cavity $r < r_f$

Wrinkles are also observed inside the cavity, unlike in the absence of a liquid substrate, a case for which they are not observed, at least for moderate impact speed (compared to the speed of sound waves in the material) [18,21]. During an experiment the number of wrinkles n observed in the cavity tends to decrease as waves propagate. The number of wrinkles is smaller inside the cavity than outside the cavity: in the last frame of Fig. 9(a), the estimated number of wrinkles is 24 inside the cavity and 42 outside (near r_f). Moreover, the variations of n with the Weber number and with the thickness h do not agree with the scaling law (23). In particular, the variation of the wavelength with the thickness of the membrane shows a much weaker variation with the thickness h, if any. Such behavior, in particular the weak dependence of wavelength on thickness, is observed for patterns selected far above the threshold of buckling in stressed membranes [25]. We propose here an analysis of the pattern for a finite amplitude of the modulation of the transverse displacement. We write the transverse displacement (at a given time)

$$w(r,\theta) = w_0(r) + f(r)\cos(n\theta). \tag{24}$$

We consider that the transverse displacement relaxes the orthoradial strain and thus that the length of a perimeter $2\pi R$ is equal to $\int [(r d\theta)^2 + (dw)^2]^{1/2}$, thus yielding

$$|\epsilon_\theta| \approx \frac{n^2 f^2(r)}{4r^2}. \tag{25}$$

This is a geometrical relation between the amplitude of the pattern f and its wave number n. After having experienced a buckling instability, the membrane is bent. The change in elastic energies associated with the wrinkling takes the form of a bending energy for which the strain is $(h\kappa_\theta)$, where $\kappa_\theta \sim (1/r^2)\partial^2 w/\partial\theta^2$ is the curvature,

$$U_b \sim \iint Y \left(h \frac{1}{r^2} \frac{\partial^2 w}{\partial \theta^2} \right)^2 r\, dr\, d\theta, \tag{26}$$
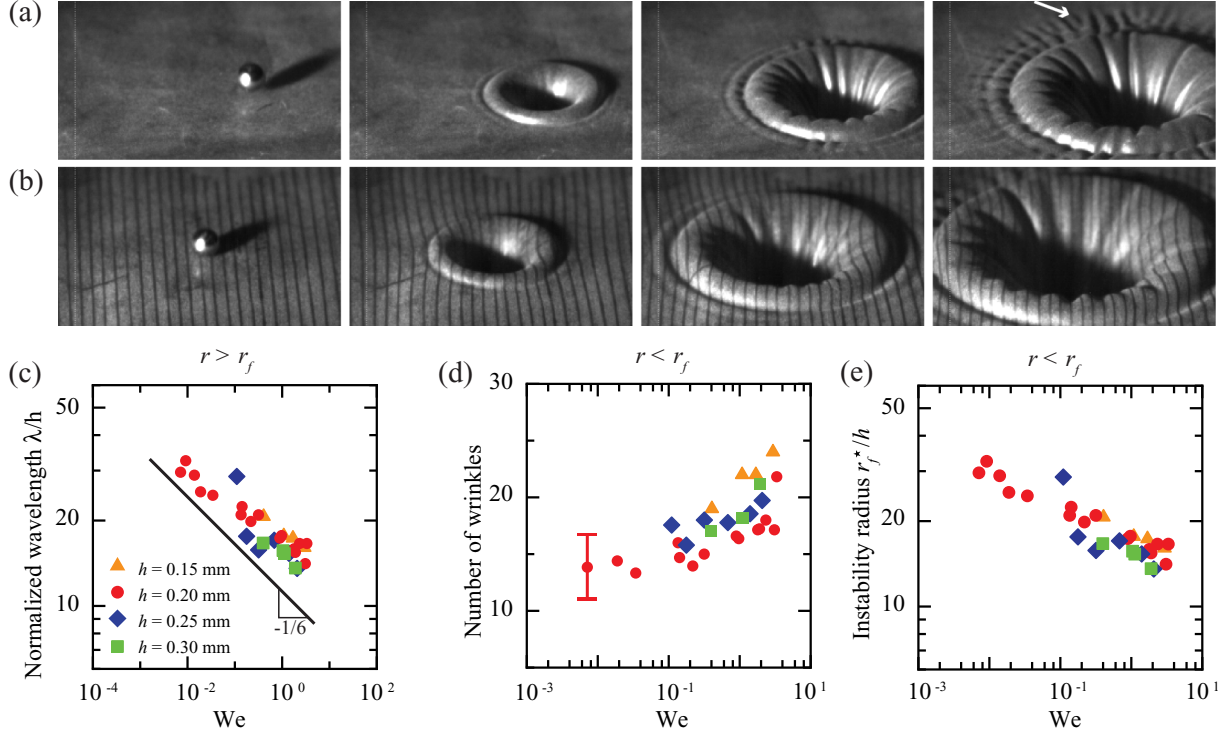
FIG. 9. (a) and (b) Dynamics of waves and wrinkling of an impacted membrane. The experimental parameters are $r_i = 2.38$ mm and (a) $V = 26.4$ m/s, $h = 0.15$ mm and (b) $V = 30$ m/s, $h = 0.30$ mm. Pictures were taken at times (a) $t = 0$, $t = 0.6$, $t = 1.4$, and $t = 2.2$ ms and (b) $t = 0$, $t = 0.6$, $t = 1.2$, and $t = 1.8$ ms. Radial wrinkles can be seen in the cavity and outside the cavity with different wave numbers. The wrinkles outside the cavity have a well-defined wavelength, and as the wave propagates, new wrinkles appear (see arrow). (c) The wavelength of wrinkles outside the cavity decreases with impact speed according to equation (23). (d) The number of wrinkles inside the cavity is different from the number of wrinkles outside the cavity. It does not exhibit a clear variation with the sheet thickness. (e) The radius r_f that has been reached by the transverse wave front when wrinkles appear in the cavity is proportional to the sheet thickness.

and a stretching energy, where the excess strain in the radial direction resulting from the nonaxisymmetric motion is proportional to $(\partial w/\partial r)^2$, and thus

$$U_s \sim \iint (Y\epsilon_s)[f'(r)\cos(n\theta)]^2 r\,dr\,d\theta. \qquad (27)$$

Denoting F as the scale for the amplitude f, we have $U_b \sim Yh^2F^2n^4/r_f^2$ and $U_s \sim Y\epsilon_sF^2$, where we have assumed that the radial variations occur with a scale r_f. Using the relation $F^2 \sim r_f^2|\epsilon_\theta|/n^2$, it appears that U_b scales like n^2 and U_s like n^{-2}. Thus the elastic energy $U_b + U_s$ is minimal when

$$n^4 \sim \left(\frac{r_f}{h}\right)^2 \epsilon_s. \qquad (28)$$

The wave number that is observed in the experiment results from the pattern that develops after the onset of instability. Wrinkling with a wave number n occurs when the stretching energy associated with compression in the orthoradial direction

$$U_\theta \sim \iint (Y\epsilon_\theta)\left[\frac{n}{r}f(r)\sin(n\theta)\right]^2 r\,dr\,d\theta \qquad (29)$$

is of the same order of magnitude as the bending energy (26). With the scaling $U_\theta \sim Y|\epsilon_\theta|n^2F^2$ one obtains an instability when $r_f^2 = r_f^{\star 2} \sim h^2n^2/|\epsilon_\theta|$. This estimation of the characteristic time at which the pattern is selected assumes that the

instability growth time is comparable to the time to reach the threshold of instability. Using $r_f^\star$ in the scaling (28) yields

$$n \sim \left(\frac{\epsilon_s}{|\epsilon_\theta|}\right)^{1/4}, \quad r_f^\star \sim h\frac{\epsilon_s^{1/2}}{\epsilon_\theta}. \qquad (30)$$

The selected number of wrinkles observed in the experiment actually shows no clear variation with the thickness h, whereas the radius at which wrinkles are observed scales linearly with the thickness, in agreement with the present analysis (Fig. 9). We note, however, that the model does not capture the weak dependence of the number of wrinkles with the Weber number: n increases with the Weber number, and $r_f^\star$ shows a variation weaker than the expected $\mathrm{We}^{-1/6}$. This discrepancy between the simplified model and the experimental results may be the consequence of higher order corrections in the ratio $\epsilon_s/\epsilon_\theta$. The quasistatic analysis used in Sec. IV indicates that the ratio $\epsilon_s/|\epsilon_\theta|$ increases weakly with the Weber number [$\epsilon_s/|\epsilon_\theta| \approx (1 + s\,\mathrm{We}^{1/3})$, where $s \lesssim 1$ is a number].

VI. DECELERATION OF THE IMPACTOR

The propagation of waves on the membrane and in the fluid is associated with a transfer of momentum from the impacting object. As a result, the impactor decelerates. The dynamics of the membrane as the sphere decelerates is shown in Fig. 10. For the three impact speeds presented in the figure, the shapes of the membrane exhibit significant differences: at low impact
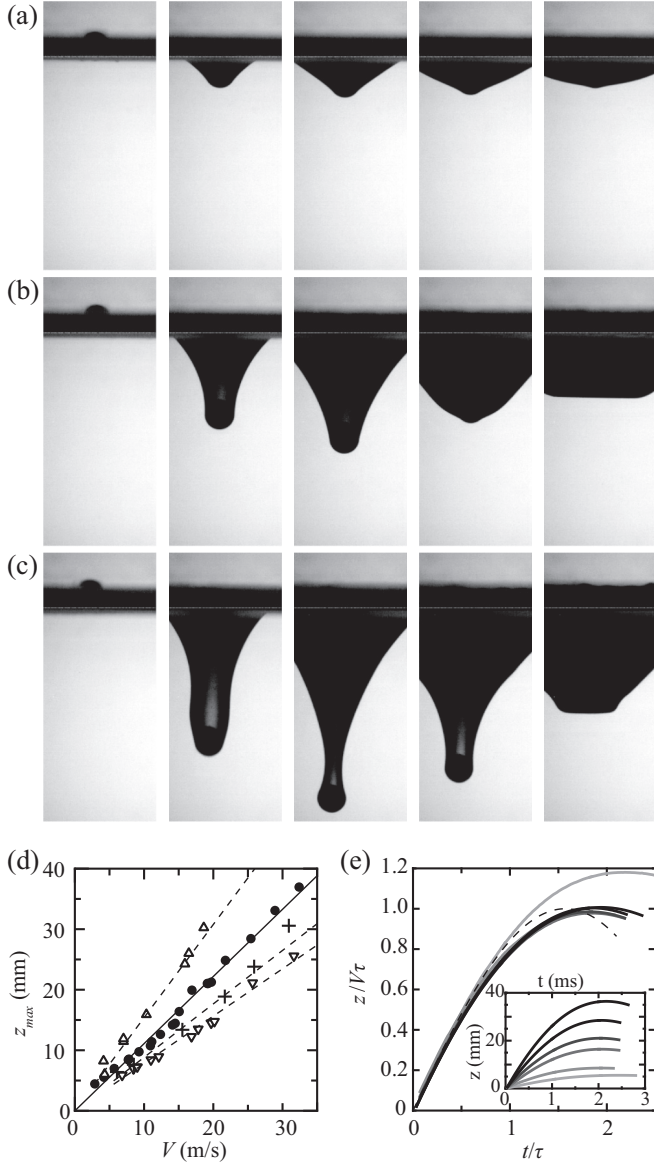
FIG. 10. Deceleration of the impactor. (a)–(c) Images of a membrane of thickness $h = 0.2$ mm as a sphere of radius 2.38 mm and mass $m = 0.44$ g impacts and decelerates. The interval between each frame is 1.07 ms. The impact speeds are (a) $V = 6.5$ m/s, (b) $V = 19.3$ m/s, and (c) $V = 32.0$ m/s. (d) Maximal penetration of spheres of radius 2.25 mm and mass $m = 0.37$ g (D1, disks), $m = 0.72$ g (D2, upward-pointing triangles), and $m = 0.18$ g (D3, downward-pointing triangles) for a membrane of thickness $h = 0.19$ mm and a sphere of mass $m = 0.37$ g for a membrane of thickness $h = 0.29$ mm (D4, crosses). The solid line is a linear fit for data set D1, and the dashed lines are deduced from the theory (see text) for data sets D2, D3, and D4. (e) When rescaled, the raw trajectories of the impactor (shown in the inset, from bottom to top, data set D1 with $V = 4.19, 7.80, 15.0, 21.0, 25.4, 33.0$ m/s) follow approximately the same dynamics. The dashed line shows the solution (33).

speeds the angle γ remains moderate, while at intermediate and high impact speeds the angle at the contact with the impactor ($r = r_i$) reaches $\pi/2$. At high impact speeds [Fig. 10(c)] the shape of the cavity is similar to the case of a nonwetting sphere impacting a water surface (except for the absence of

pinch-off) [2]. This behavior is characteristic of high Weber numbers (here We = 3.4). After impact, the sphere decelerates until it stops and then rebounds. Figure 10(d) shows that the maximal penetration grows linearly with the impact speed. For moderate and high speeds, the time at which the maximal penetration occurs does not change significantly with impact speed, as seen in the inset of Fig. 10(e), where the vertical position of the impactor has been plotted as a function of time for different values of the impact speed.

In order to make a simplified analysis of the motion of the sphere, we write the equation for the position z of the impactor,

$$m \frac{d^2z}{dt^2} + F_i = 0, \tag{31}$$

where m is the mass of the impactor and F_i is the force exerted by the impactor on the membrane. The simplest form for the force is to assume a quasistatic behavior of the membrane and to write the force

$$F_i = 2\pi r_i Y \epsilon_i \sin \gamma(r_i, t) \approx 2\pi Y k z(t), \tag{32}$$

where we have used the results of Sec. IV, $\epsilon_s(r_i, t) = kVt/r_i$, with $Vt = z(t)$ and $k = \mathcal{E}_s(1)$. We have also made the approximation $\sin \gamma(r_i, t) = 1$, which is valid if the impact speed is not too small. Most importantly, we have assumed that the pressure impulse occurring just after impact could be neglected in comparison with the tension in the membrane. This hypothesis comes from the fact that the impact force scales like r_i^2, whereas the tension scales like r_i. As a consequence, we expect F_i to be much larger than the impact force as soon as ϵ_i is non-negligible.

This simplified model with a Hookean restoring force yields a solution with initial conditions $z(0) = 0$ and $dz/dt(0) = V$,

$$z(t) = V\tau \sin \left(\frac{t}{\tau} \right), \quad \tau = \left(\frac{m}{2\pi Y k} \right)^{1/2}. \tag{33}$$

The time scale obtained from the experiments, shown as the slope of the curves in Fig. 10(d), is in fair agreement with the time scale deduced from the quasistatic model: for data set D1, we find $\tau \approx 1.11$ ms from the experiments [solid line in Fig. 10(d)], which yields $k \approx 0.070$, in fair agreement with $k = \epsilon_s(r_i, t) r_i / Vt = \mathcal{E}_s(1) \approx 0.05$, as seen in Fig. 8. With $k \approx 0.070$ the other data sets are well approximated by the lines $z_{\max} = V\tau$ [shown as dashed lines in Fig. 10(d)], where τ is computed from Eq. (33) with the corresponding values of the mass m and thickness h. Solution (33) is in qualitative agreement with the rescaled experimental curves [Fig. 10(e)], apart from the position of the maximum. We also note that a discrepancy is observed for the lower speeds, caused by the variations of γ not accounted for in the simplified model. It is also worth mentioning that after its deceleration, the sphere is accelerated by the membrane and finally ejected. Therefore we can measure a coefficient of restitution. The deceleration and rebound dynamics is presented in Fig. 11. The coefficient of restitution increases with impact speed and seems to have an asymptotic finite value as $V \to 0$. These features are also observed in the case of impact of nonwetting spheres on a water surface [26].

It is interesting to compare the dynamics of the floating membrane to the case of an impacted plate. In the present case, the stretching at the contact with the impactor, which
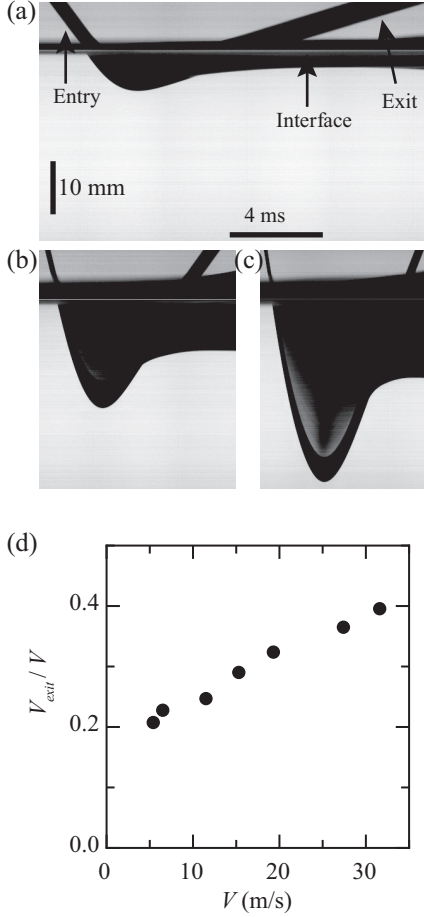
FIG. 11. (a)–(c) z-t diagrams showing the entry at velocity V, deceleration, and exits at velocity V_{exit} of a sphere corresponding to the images in Fig. 10. (d) The coefficient of restitution varies with the impact speed.

will ultimately (for high speeds) be responsible for the puncturing of the membrane, increases progressively with time with a time scale r_i/V, while the deceleration occurs at a time scale $\sim (m/Y)^{1/2}$. This is different from the case of an impacted plate of thickness h, characterized by its bending rigidity, where the nominal curvature $V/(ch)$ is reached very rapidly, within the short time necessary to establish the Hertzian response of the plate: this time is typically $t_H \sim (h/c)(c/V)^{1/3}(h/r_i)^{1/3}$ [27].

VII. CONCLUSIONS

We have studied the behavior of a membrane floating on a liquid pool impacted by a rigid object. The membrane is initially stress free. Tension in the membrane develops as a result of the impact, and the dynamics of the transverse wave is coupled with the tension wave. We have shown that the strain distribution, and therefore the stress distribution, observed in the experiments on the membrane is fully consistent with a simplified theoretical model. This model consists of the assumptions that the transverse wave front travels in the radial direction with a $t^{2/3}$ law and that the membrane is, at each instant, in internal equilibrium. This model allowed us to describe the shape of the membrane in the region of

the transverse wave as a self-similar function, analogous to surface-tension-dominated free-surface flows. The equivalent local surface tension coefficient, derived from the theory, is constant in time and increases like the Weber number to the power of $1/3$, as observed in the experiments. Moreover, the theoretical expression for the strain in the transverse wave region gives a scaling for the wavelength of the wrinkles observed at long times, which is in agreement with the experiments. Finally, the model allows us to understand the deceleration of the impactor: the agreement between the theory and the experiments is fairly good for this purpose.

We leave here, as a perspective of this work, a deeper experimental study of the deceleration of the impactor and the wrinkle growth. In order to conclude on this aspect, we shall need to change the material properties (thickness of the membrane and Young's modulus, although the domain of variations is limited by the bending response that will unavoidably affect the wave dynamics for thick or rigid membranes) and the liquid properties (density, kinematic viscosity) in order to disentangle this complex long-time dynamics. One remaining open question that this future work should address is the amount of energy transfer during the impact. Indeed, quantifying the energy transferred into kinetic energy (inside the fluid) and elastic energy (in the membrane) should have many applications.

APPENDIX: SELF-SIMILAR SYSTEM OF EQUATIONS

The self-similar ansatz for the velocity potential, the pressure jump across the membrane, the vertical displacement, and the two strains are

$$\phi(r,z,t) = a^2 t^{1/3}\Phi(\xi,\zeta), \quad p(r,z,t) = \rho a^2 t^{-2/3}P(\xi,\zeta),$$

$$w(r,t) = \eta a t^{2/3}W(\xi), \quad \epsilon_s = E_s(\xi), \quad \epsilon_\theta = E_\theta(\xi), \quad \text{(A1)}$$

where $\xi = r/r_f$, $\zeta = z/r_f$, $a = (Y\epsilon_f/\rho)^{1/3}$. Plugging these expressions into mass conservation and Eqs. (5), (6), and (11)–(14), we obtain the following set of equations:

$$\Delta\Phi = 0 \quad \text{(A2)}$$

for $\zeta \leqslant W(\xi)$ and

$$\frac{2}{3}\eta W(\xi) - \frac{2}{3}\eta \xi W'(\xi) = \Phi_\zeta - \eta W'(\xi)\Phi_\xi,$$

$$\frac{1}{3}\Phi - \frac{2}{3}[\xi\Phi_\xi + \eta W(\xi)\Phi_\zeta] + \frac{1}{2}\nabla\Phi^2 + P = *0,$$

$$\frac{d}{d\xi}\left[\xi\left(E_s + \frac{E_\theta}{2}\right)\right] - \left(E_\theta + \frac{E_s}{2}\right) = 0,$$

$$\frac{\xi}{1+E_\theta}\frac{dE_\theta}{d\xi} + \frac{1+E_\theta}{1+E_s}\sqrt{1+\eta^2 W'^2(\xi)} = 1,$$

$$\left(E_s + \frac{E_\theta}{2}\right)\frac{d\gamma}{d\xi} + \left(E_\theta + \frac{E_s}{2}\right)\frac{W'(\xi)}{\xi}$$

$$+ P\sqrt{1+\eta^2 W'^2(\xi)} = 0$$

for $\zeta = W(\xi)$

[1] A. M. Worthington, *A Study of Splashes* (Longmans, Green, London, 1908).

[2] V. Duclaux, F. Caillé, C. Duez, C. Ybert, L. Bocquet, and C. Clanet, J. Fluid Mech. **591**, 1 (2007).

[3] J. M. Aristoff and J. W. M. Bush, J. Fluid Mech. **619**, 45 (2008).

[4] C. M. Seddon and M. Moatamedi, Int. J. Impact Eng. **32**, 1045 (2006).

[5] T. von Kàrmàn, *The Impact on Seaplane Floats During Landing*, Technical Report NACA-TN-32 (National Advisory Committee for Aeronautics, Washington, DC, 1929).

[6] H. Wagner, Z. Angew. Math. Mech. **12**, 192 (1932).

[7] O. Faltinsen, *Sea Loads on Ships and Offshore Structures* (Cambridge University Press, Cambridge, UK, 1993), Vol. 1.

[8] J. W. Bush and D. L. Hu, Annu. Rev. Fluid Mech. **38**, 339 (2006).

[9] D. Vella and P. D. Metcalfe, Phys. Fluids **19**, 072108 (2007).

[10] H. M. Lund and S. B. Dalziel, J. Fluid Mech. **756**, 771 (2014).

[11] J. Lucassen, Trans. Faraday Soc. **64**, 2221 (1968).

[12] J. Lucassen, Trans. Faraday Soc. **64**, 2230 (1968).

[13] Y. Couder, J.-M. Chomaz, and M. Rabaud, Phys. D (Amsterdam, Neth.) **37**, 384 (1989).

[14] K. H. Christensen, Phys. Fluids **17**, 042102 (2005).

[15] K. F. Graff, *Wave Motion in Elastic Solids* (Dover, New York, 1975).

[16] K. A. Rakhmatulin and Y. A. Dem'yanov, Strength under High Transient Loads [English translation, Israel Program for Scientific Translations, Jerusalem, 1966].

[17] S. L. Phoenix and P. K. Porwal, Int. J. Solids Struct. **40**, 6723 (2003).

[18] R. Vermorel, N. Vandenberghe, and E. Villermaux, Proc. R. Soc. A **465**, 823 (2009).

[19] L. Duchemin and N. Vandenberghe, J. Fluid Mech. **756**, 544 (2014).

[20] J. B. Keller and M. J. Miksis, SIAM J. Appl. Math. **43**, 268 (1983).

[21] A. B. Albrecht and K. Ravi-Chandar, J. Mech. Phys. Solids **64**, 377 (2014).

[22] E. Cerda and L. Mahadevan, Phys. Rev. Lett. **90**, 074302 (2003).

[23] J. Huang, M. Juszkiewicz, W. H. de Jeu, E. Cerda, T. Emrick, N. Menon, and T. P. Russell, Science **317**, 650 (2007).

[24] L. D. Landau and E. M. Lifshitz, *Theory of Elasticity*, Course of Theoretical Physics Vol. 7 (Pergamon Press, Oxford, 1986).

[25] G. M. Grason and B. Davidovitch, Proc. Natl. Acad. Sci. USA **110**, 12893 (2013).

[26] D.-G. Lee and H.-Y. Kim, Langmuir **24**, 142 (2008).

[27] C. Zener, Phys. Rev. **59**, 669 (1941).